Liquid Crystals

ISSN: (Print) (Online) Journal homepage: https://www.tandfonline.com/loi/tlct20

Nanosecond illumination source for speckle-free liquid crystalmicroscopy

A. V. Ryzhkova, U. Jagodič & Igor Muševič

To cite this article: A. V. Ryzhkova, U. Jagodič & Igor Muševič (2021) Nanosecond illumination source for speckle-free liquid crystalmicroscopy, Liquid Crystals, 48:4, 491-510, DOI: 10.1080/02678292.2020.1790049

To link to this article: https://doi.org/10.1080/02678292.2020.1790049

LIQUID CRYSTALS
2021, VOL. 48, NO. 4, 491–510
https://doi.org/10.1080/02678292.2020.1790049

Taylor & Francis
Taylor & Francis Group

Nanosecond illumination source for speckle-free liquid crystal microscopy

A. V. Ryzhkova[a], U. Jagodič[a] and Igor Muševič[a,b]

[a]Condensed Matter Department, Jožef Stefan Institute, Ljubljana, Slovenia; [b]Faculty of Mathematics and Physics, University of Ljubljana, Ljubljana, Slovenia

ABSTRACT

We present a setup for the speckle-free, low-light microscopy imaging at ~5 ns exposure times. The design is based on stroboscopic principle and uses fast and incoherent fluorescent emission from a dye, excited by a picosecond laser pulse. The basic spatial, spectral, and temporal beam properties are characterised, modelled and compared for two different designs of the source: (i) Rhodamine 6 G dye dissolved in ethanol and put in a glass cuvette, and (ii) random laser based on the dispersion of 300 nm TiO_2 nanospheres in an ethanol solution of Rhodamine 6 G dye. The proposed solution of Rhodamine 6 G dye in ethanol put in a glass cuvette gives an excellent image quality with high contrast, excellent stability and tunable coherence. It delivers ~30 nJ of completely incoherent light per excitation laser pulse energy of ~40 μJ. It allows for the photographic measurements with 5 ns exposure time, demonstrated in imaging of thermally quenched 5CB liquid crystal. The set-up is used in studies of Kibble-Zurek mechanism of topological defect nucleation and growth at sub-microsecond time resolution and extremely fast cooling rates of ~40,000 K/s.

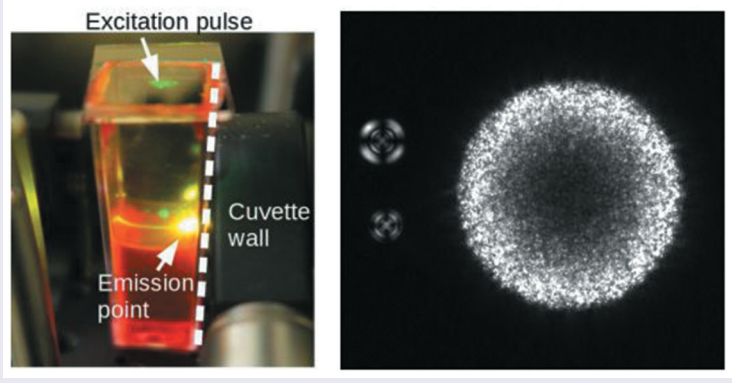

ARTICLE HISTORY
Received 28 February 2020
Accepted 28 June 2020

KEYWORDS
Nanosecond illumination; liquid crystals; speckle-free illumination; Kibble-Zurek mechanism

1. Introduction

During recent years unique methods have been developed to take images of fast and ultrafast phenomena [1]. Continuous imaging methods such as Single-shot Shadowgraphy (SS) [2], Serial Time-Encoded Amplified imaging/Microscopy (STEAM) [3,4], Single-shot Multispectral Tomography (SMT) [5], Fluorescent Imaging by Radiofrequency-tagged Emission (FIRE) [6,7] provide continuous acquisition mode with a frame rate of 1 kfps – 10 Mfps and exposure time of 100 fs – 100 μs. Sequential Timed All-optical Photography (STAMP) [8,9], Frequency-Domain Tomography (FDT) [10,11] and Compressed Ultrafast Photography (CUP) [12] can provide a limited total number of frames (burst data) with a frame rate of 100 Gfps – 1 Tfps and exposure time of 1 ps – 10 ps. These techniques have overwhelming specifications with respect to the number of acquired frames and exposure durations, but suffer from high costs, design complexity of the optical system, and computational costs, requiring real-time digital processing. Furthermore, these imaging methods are using fast or ultra-fast powerful lasers as an illumination source, and the acquired images show speckles due to the inherent coherence of lasers. The acquired images are therefore not suitable for applications, where a high-quality image without any trace of speckles is required.

Single imaging technique (or stroboscopic imaging technique) [13–15] is a very simple and efficient method in observing fast processes. It has relatively low costs, simple optical design, and good image quality.

CONTACT Igor Muševič igor.musevic@ijs.si Condensed Matter Department, J. Stefan Institute, Jamova 39, SI-1000, Ljubljana, Slovenia

Unfortunately, this method is limited by a single available frame and the illumination is performed by a single laser or a diode pulse. The number of frames can be increased to few in case of the beam split and pulse delaying, such as in pump-probe and shadowgraphy techniques [16] or in case of triggering several lasers with pre-defined delays [17,18].

We are interested in speckle-free, high optical quality stroboscopic imaging, which is capable of capturing a single image using a high-quality optical microscope (e.g. Nikon Eclipse) with 60 or 100 × objective and highly sensitive, low noise CMOS camera (e.g. Andor Neo). Such stroboscopic imaging requires a fully incoherent light pulse of typically 10 ns duration, which can deliver ~60 nJ energy per light pulse to the CMOS sensor of the camera. This is typical energy, which is required to fully saturate the CMOS sensor of a high-quality CMOS camera.

There are not many pulsed light sources available that would meet these specifications. LED-light sources are a perfect choice for an incoherent illumination strobe, with no coherence and practically absent pulse-to-pulse intensity variations. Commercially available LEDs can give pulse energy equivalent to 2000 W for a 256 mm^2 area of emission and strobe time duration of several microseconds [19]. Commercially available LED illumination sources for optical microscopes (e.g. Cool LED) can deliver several μJ of energy, but the pulse duration is rather long ~40μs. Current development trends show that high-power LED devices provide sufficient light and could be suitable for fast phenomena diagnostics [20–22]. However, there are challenges to be solved, like wide-angle radiation pattern (i.e. high N.A.) [20]. Until now it is not clear whether currently available high speed LED strobes, with its fall and rise times in the nanosecond range [23], could provide sufficient light for a low-light-level applications.

Quite recently random lasers [24,25] were proposed for sub-nanosecond imaging, because they generate very bright and short illumination pulses. In a random laser, light is generated within a positional disordered system, such as a random dispersion of small dielectric spheres in a solvent with a fluorescent dye. The dye provides optical amplification and the laser resonator is, in fact, a virtual resonator, formed by multiple scattering of photons from micro-particles. The resonance condition is fulfilled for a given closed path generated by a sequence of scattering of photons from the dispersed particles. Such a multimode laser exhibits high brightness but suffers from partial coherence, an inherent property of amplification of light by stimulated emission.

Finally, another appealing approach is to use incoherent fluorescent emission from a dye, excited by a powerful pulsed laser, thus converting coherent laser light into a speckle-free illumination source. The idea is not new [26], and conversion efficiency of ~10% has been claimed. Multiple design solutions for the wavelength converters based on films, bulbs, and cuvette containing dye are known [26–28]; however, there is little evidence on the real characteristic of such an illumination source.

This work was stimulated by our recent experiments on extremely rapid cooling of a liquid crystal across the isotropic-nematic phase transition [29]. In a broader context, we aim at imagining the emergence of topological defects at a predefined time after the beginning of cooling. The emergence and evolution of defects are imaged using nanosecond illumination system, synchronised with the time, when the cooling starts. Therefore, we take ”instantaneous” images of defects at a certain (i. e. predefined) time delay after the quench is initiated. By performing a number of separate experiments with different delay times after the quench, we get a ”movie” of defect evolution in the sense of defect statistics, such as their density, brightness and size distributions.

Because the achieved cooling rates are extremely fast, i.e. of the order of 10.000 K/s, the imaging of emerging defects needs to be done in a time, preferably much shorter than one microsecond. There are not many options left and we decided to explore properties of fluorescent sources, excited by a strong and short laser pulse. The main goal of this work was to design and test nanosecond illumination source with high brightness and low level of coherence based on light emission from a dye, which is excited by a laser pulse. We present a design solution for the good-quality (i.e. low level of speckles) light source for photographic measurements of fast phenomena with 5 ns full width at half-maximum (FWHM) exposure light pulse. We show that fluorescent emission of an organic dye pumped with the high energy laser pulse provides very high photon emission flux, sufficiently bright to be used for crossed-polarised optical microscopy. The spectral, temporal and coherence properties of this light source are compared with a random laser, made from the same dye dissolved in ethanol dispersion of 300 nm TiO_2 nanoparticles.

2. Materials and methods

The principle of the set-up is based on a stroboscopic technique, using a broadband light pulse, generated from a fluorescence dye, for specimen illumination. The light pulse is obtained from a fluorescent

conversion of a single 30 ps laser pulse into a broadband incoherent light pulse. The duration of visible light pulses generated from fluorescent dye is 5–20 ns (FWHM) and is determined by the fluorescent lifetime of the dye. The set-up is schematically shown in Figure 1 and consists of four basic parts: (i) wave-length converter, (ii) illumination optics, (iii) imaging optics and (iv) system for thermal quenching.

2.1. Fluorescent light converter

The experimental set-up is presented in Figure 1. We use a mode-locked picosecond Nd: YAG laser PL2251A-10 (Ekspla) to generate up to 50 mJ light pulses at λ= 1064 nm and 30 ps duration. The 8 mm beam is converted into a second harmonic 30 ps laser light pulse at λ= 532 nm using the SH generator (H400FH, Ekspla). The energy of the SH pulses is varied in the range of 0.1–10 mJ during the operation, the maximum possible level is up to 20 mJ. The green light is guided through the set of mirrors and is narrowed from 8 mm beam diameter into 1 mm diameter beam using a pair of lenses L1 and L2, see Figure 1. The green laser beam is slightly focused onto the surface of the Rhodamine 6 G (Rh6 G) dissolved in ethanol (C_2H_5OH) contained in the glass cuvette. The diameter of the green pumping beam at the Rh6 G-air interface is around 1 mm. If stronger focusing is used, the dye is burnt by the high energy pumping light. The concentration of the dye is 0.01 mol/l and the total solution volume is 2.6 ml. The depth of penetration of a laser light into a solution can be calculated using the Beer's law. The law states that the optical absorbance of a fluorophore in a transparent solvent varies linearly with both the concentration of the dye and the sample cell path length. The absorbance (A_λ) is calculated from the logarithm of the ratio of the light intensity, that is incident on the sample cell (I_0) and the intensity passing through the sample cell (I) is $A_\lambda = log(I_0/I)$. The absorbance of a sample depends on the molar concentration ($c, [mol \cdot L^{-1}]$), length of solution the light passes through (L, [cm]), and molar absorbance (ε, $[L \cdot mol^{-1} \cdot cm^{-1}]$) for the dissolved substance, $A_\lambda = \varepsilon \cdot c \cdot L$.

For Rh6 G illuminated at 532 nm, $\varepsilon(532nm) = 114441 M^{-1}cm^{-1}$. In the experiment, 11 mg of Rh6 G is dissolved in 2.6 ml of ethanol, resulting in molar concentration of $c = m/(VMW)$= 0.0094 M/l. Here MW= 479.02 g/M is the molecular weight of Rh6 G.

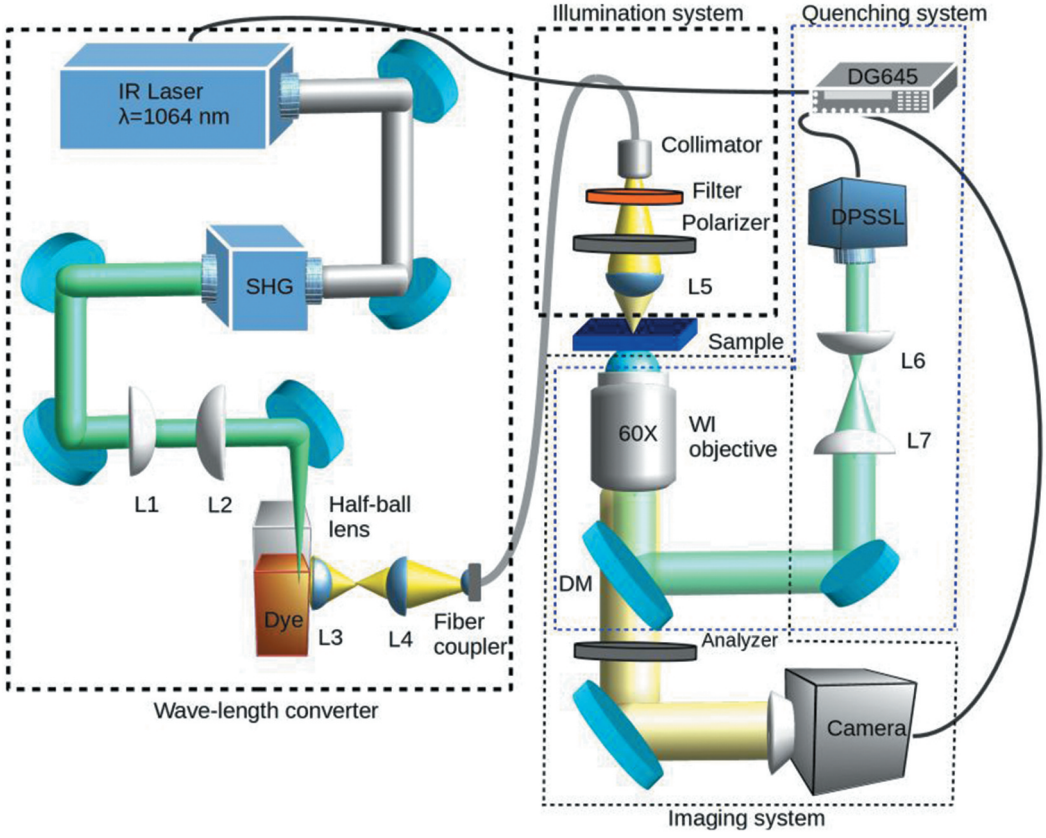

Figure 1. (Colour online) The experimental set up consists of the four sub-systems: the wave-length converter, the illumination system, the imaging unit and the system for inducing fast temperature quench of the sample.

We calculate the thickness of the sample cell L, over which the 532 nm light pulses are attenuated, for example, thousand times I/I_0= 0.001, and we obtain $L = A_\lambda/(\varepsilon \cdot c) = 27.7 \cdot 10^{-4} cm \approx 30\mu$m.

The prepared volume of the dye-ethanol solution is sufficient for 3 weeks ($\approx$ 4.3 million pulses) of continuous operation. In $\approx$ 4.3 million pulses of operation, the fluorescent dye fully photo bleached. The gradual photo-bleaching of the dye is compensated by the corresponding increase of the pumped energy of the SH up to 20 mJ before the sample becomes fully bleached.

The geometry of this wavelength converter is shown in Figure 1. The pumping laser light is slightly focused by lenses L1 and L2, forming a 1 mm diameter spot at the surface of Rh6 G solution. This spot is positioned close to the wall of the cuvette, enabling efficient coupling of fluorescent emitted light into a lens system for collecting the fluorescent light (L3 and L4). In some cases, the excitation spot is positioned far away from the wall of the cuvette, influencing the amount of collected light and its coherence, as shall be analysed in the continuation. The fluorescent light is collected only from a thin layer at the dye-cuvette interface by a 4 mm half-ball lens (wavelength range 350–2200 nm, Edmund Optics) and is imaged into a tiny spot of about 1 mm size. The obtained image of the emitting fluorescent layer is projected into the fibre coupler (PAF–SMA–7–A) by using a lens (L4) with 10 mm focal distance. The multi-mode fibre is guiding the fluorescent light further into the illumination system. After propagating 2 m distance through the fibre, the beam profile obtains the super-Gaussian shape and the former beam shape imperfections of the original beam are eliminated to a great extent.

2.2. Random laser converter

Spectral and temporal properties of fluorescent light, generated from Rh6 G solution, are compared to the light emitted from a random laser, made of the same dye and following the design in Ref [24]. Glass cells are made of two soda-lime glass plates glued together to form a sandwich with 170μm gap thickness. The cell is filled with a colloidal suspension containing 406 mg of 300 nm nanobeads of TiO_2 (rutile, high purity, 99.9%, US Research Nonmaterials) in a laser dye solution 15.7 mg of Rh6 G dissolved in 3.5 ml of ethanol. The concentration of Rh6 G in ethanol is kept similar as for the fluorescent light converter. The random lasing is excited by focusing the green excitation beam along the direction, perpendicular to the cell plates. The emitted light from the random laser is coupled from the side of the cell, as presented in Figure 2. Although this is not an optimum output coupling for a random laser, it generates sufficient light intensity for the purpose of analysing spectral, temporal and coherence properties of random laser converter.

2.3. Illumination and imaging system

The illumination system consists of a collimator with a numerical aperture (NA) of 0.15, notch filter (λ= 532 nm with FWHM of 17 nm, Thorlabs), a polariser and a lens (L5) with 10 mm focal distance. The lens (L5) is positioned on a 3D-stage, enabling accurate lens alignment with respect to the microscope optical axis. Alignment of the lens (L5) and the collimator with respect to each other and microscope axis is very important because it can cause beam aberrations and imaging artefacts as well as a mismatch between image planes of the built-up illumination system and an objective. Adjustment of the lens in the z-axis (along beam propagation direction) enables variation of the illumination spot intensity and its size according to the viewing area of an objective. A rotating polariser is positioned between the notch filter and focusing lens (L5).

The imaging system is built up from a water immersion Nikon objective NIR APO 60 × 1.0 W DIC N2 WD 2.8, analyser and Andor Neo camera (pixel size is 6.5 μm), as presented in Figure 1. A large sensor dimension of 16.6 mm × 14 mm of the camera enables observation of the large area in the studied sample up to ~280μm × 230μm and provides a pixel resolution of 100 nm.

2.4. Liquid crystal sample

In our experiments, we are imaging samples of a nematic liquid crystal, sandwiched between two glass plates and positioned on a 2D-stage of Nikon Eclipse Ti Microscope. The cells containing the liquid crystal are assembled from 0.7 mm thick glass plates with a 10 nm Indium Tin Oxide (ITO) layer. The liquid crystal layer is 12 μm thick and aligned with the optical axis perpendicular (homeotropic) to the plates of the glass cell. The purpose of the ITO layer is to absorb a focused DPSSL laser light and increase the local temperature of the liquid crystal above the phase transition temperature, thus forming localised island of molten (isotropic) nematic liquid crystal. Strong homeotropic surface anchoring of the nematic LC molecules is ensured by covering the glass substrates with N,N-dimethyl-n-octadecyl-3-aminopropyl-trimethoxysilyl chloride (DMOAP). The glass substrates are placed in 2% DMOAP-water solution and

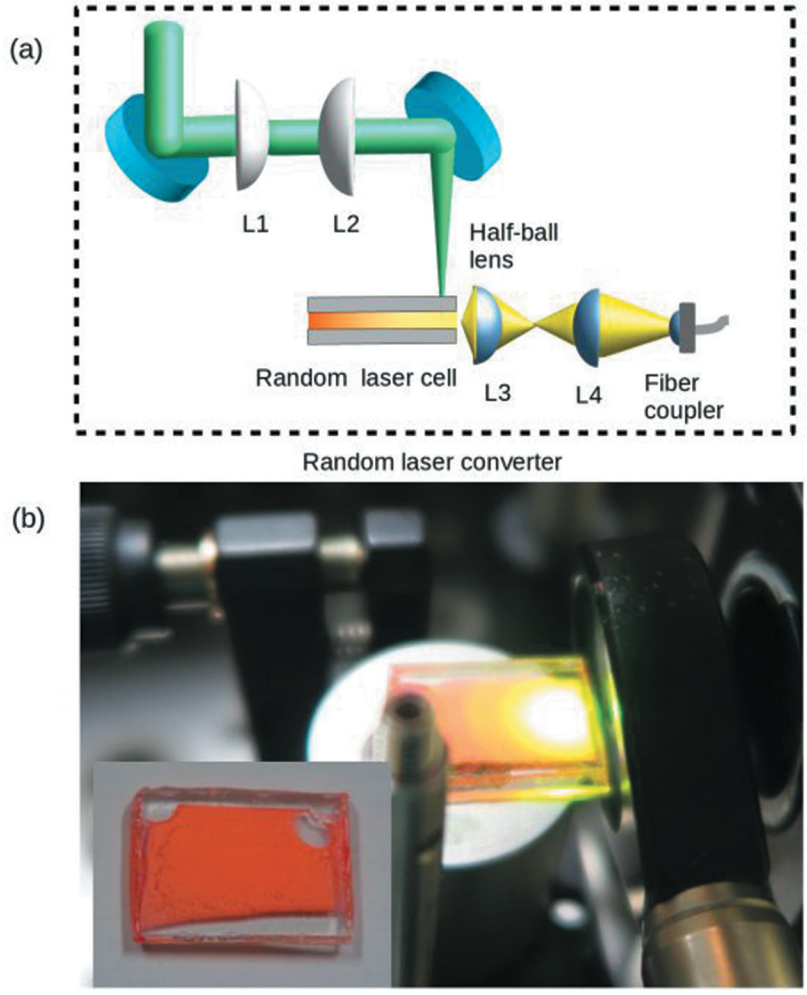

Figure 2. (Colour online) (a) Schematic details of random laser light converter. The random laser glass cell replaces the glass cuvette used for pure Rh6 G solution. (b) Photo of the random laser in operation. The coupling of the emitted light from random lasing cell into the optical fibre can be seen. The inset shows the photo of the random laser cell.

mixed for 5 min. DMOAP chemically bonds to the glass surfaces forming a well-defined monolayer. Afterwards, the glass substrates are washed with distilled water several times in order to remove the excess of the DMOAP and dried for 20 min at 120°C. The cell is filled with 4-n-pentyl-4-cyanobiphenyl (5CB) liquid crystal mixed with 10μm silanized silica micro-spheres, prepared in the same way as the glass substrates. The microparticles help finding the focal plane in the LC cell. The large birefringence of the 5CB liquid crystal (Δ n = 0.20 $\pm$ 0.02) enables high contrast imaging of the defects in the cell between crossed polarisers.

2.5. Quenching system

The purpose of the quenching system is to provide controlled heating of the sample via absorption of the laser light in the ITO layers of our liquid crystal cells. The absorbed light increases the local temperature of the liquid crystal and creates a small island of the molten liquid crystal in the centre of the cell. After switching-off the light, this molten island rapidly cools down through the isotropic-nematic phase transition and creates topological defects.

The main part of the quenching system is an externally controlled solid-state laser DPSSL MGL-III emitting 532 nm laser line, with an actual operational power of 120 mW in the continuous mode. The output beam size is $\sim$1 mm in diameter. The laser is guided to the backside of Nikon Eclipse microscope via a set of mirrors. A dichroic mirror (AHF F73-816, DM in Figure 1) is used to direct the λ= 532 nm laser light trough a water immersion objective onto the sample. A pair of lenses (L6 and L7) is inserted in the beam path to expand the beam size to $\sim$3 mm in diameter, such that at the focus of 60 $\times$ WI objective the spot size is $\sim$50μm.

The heating laser is turned on for 30 ms every 2.1 s. This duty cycle provides thermal equalisation of the sample between experiments, preventing local overheating

and damage of the alignment layers in the LC cell. The measured delay and rise time of the DPSSL laser used for heating is 100μs and the fall time is 20μs, both negligibly small with respect to the pulse duration of 30 ms. By considering the CW laser operation power of 120 mW, and the 30 ms illumination time, the delivered laser energy is around 3.6 mJ. Only about one half of that energy reaches the sample due to the optical losses along the beam path, achieving the delivered energy of ~1.8 mJ, which is available of heating and melting the liquid crystal. The fluence at the focal point is $E/2/(\pi r^2) or E/(2\pi r^2)$, where $r \approx 25\mu$m is a radius of the beam spot at the ITO layer. Factor of two is added because the Gaussian shape the heating beam varies from the rectangular one, required for fluence calculation. Therefore, the heating beam fluence is equal to 180 J/cm^2 at the heating beam focus.

The liquid crystal and alignment layer are mostly transparent for visible wavelengths and the reflectivity and absorption are due to the ITO layer. A 10 nm thick ITO layer on glass has ~4% reflectivity and a 50 nm thick ITO layer on glass reflects ~12% of light. Yet, due to the very high intensity of heating laser light, already a small amount of absorbed laser light on the ITO covered glass results in the local heating of the ITO layers. As a consequence, the liquid crystal starts locally melting, forming an isotropic island. The equilibrium diameter of the island depends on the delivered energy and thermal properties of the measuring cell, thoroughly analysed in our recent publication [29]. Briefly, the diameter of the isotropic island depends on the liquid crystal used and is around ~100μm for 5CB at 100 mW power of the heating laser. At this power level, the temperature in the centre of the isotropic island is around ~100°C°. When the heating light is switched off, the centre of the island is cooling down at a rate of up to ~40.000 K/s, resulting in an enormously fast quench rate 100 um as in micrometer [29].

2.6. Timings and delays

Timings and delays between different subunits of the experimental setup are presented in Figure 3. Delays among the setup entities are controlled by a very precise 8-channel pulse delay generator DG645 with jitter < 100 ps. It is preferable to use the main Ekspla laser unit as the generator of the trigger pulse. In the opposite case when the Ekspla laser is triggered by the external delay generator, an uncontrolled jitter might be introduced during the creation of the laser pulses. Therefore, the Ekspla laser was in the free-running mode generating the light pulses at a frequency of 10 Hz. In this mode, Ekspla is generating a 100 ns trigger pulse at the repetition rate of 10 Hz, which is followed by the light pulse after a fixed delay of 580 ns. We have measured the jitter between the trigger pulses and the light pulses and it is of the order of 1 ns only.

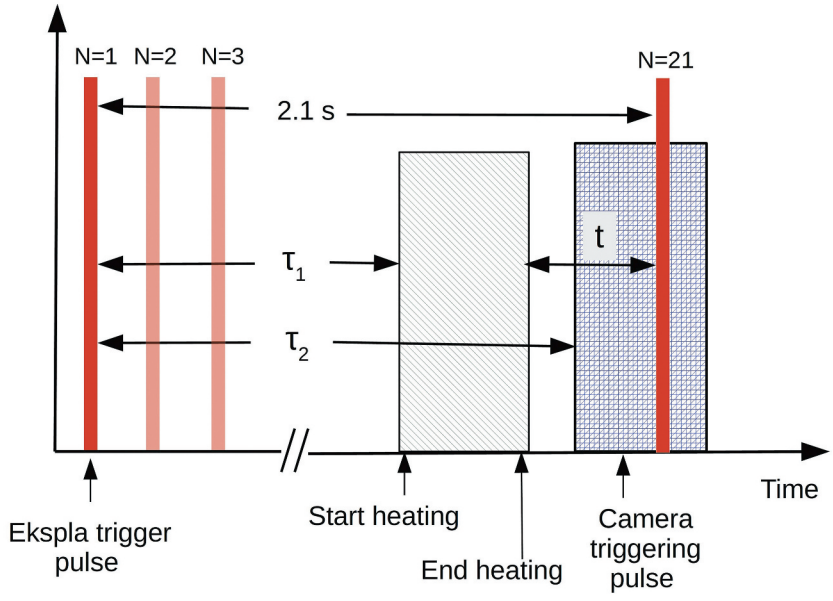

Figure 3. (Colour online) Timing and delays for the triggering of sub-systems: Ekspla laser (main unit), heating laser and Andor Neo camera. The Ekspla laser is free running at the frequency of 10 Hz, generating trigger pulse every 100 ms. The heating pulse is applied after delay time τ_1 and the image is taken using 21st light pulse as the illumination pulse. This makes the total time of a single experiment equal to 2.1 s. Faster repetition of the heating pulse results in gradual heating and overall increase of the sample temperature.

After the triggering pulse is generated by the Ekspla laser, the delay generator triggers the DPSSL laser used for heating (with delay time τ_1) and then triggers the exposure of Andor Neo camera for capturing the images (with the delay time τ_2). We take an image at the time when the 21st Ekspla pulse is generated, i.e. with a time delay of 2 s and 100 ms after the first Ekspla pulse, as shown in Figure 3. After the DPSSL laser receives the triggering pulse, delayed for τ_1, it generates a laser heating pulse with a rising time of ~100 *mu*us as in micro seconds, which lasts typically for 30 ms before it is rapidly switched off. The switching-off of the heating laser is the crucial time for our experiments, because this is the time which defines the start of cooling. We have measured that the heating laser shuts down in ~20μs, which is also acceptable for the time-resolution of our experiments. The jitter in the switching-off of the heating laser is around 400 ns.

Similarly, the Andor camera receives a triggering pulse after a delay time τ_2, and then it starts collecting light within a time interval of 1 ms. During this "active" state of Andor camera, the sample is illuminated with a fast light pulse (the 21st light pulse) and the image is recorded. Because the camera receives light only from the very short illumination pulse, very sharp and precisely defined images can be obtained. The schematics of the timing of different triggering pulses is shown in Figure 3. All delays are monitored via Infinium – MS09404A Multi Signal Oscilloscope (Agilent Technologies).

In order to capture the image in the experiment, it is necessary that the broadband fluorescent light pulse arrives to the sample at the time when Andor camera is triggered and ready to take the image within its 1 ms capturing time. For the physics of our experiment, the most important is the elapsed time t, between the end of the heating pulse and the fluorescent light pulse (see Figure 3). This is the time interval between the start of cooling of the sample and the moment, when the image is taken by a nanosecond illumination pulse. This time is calculated by subtracting from the total time of 2 s 100 ms the delays and durations of the quenching pulse. By varying the delay time τ_1 one could change the elapsed time t, when the defect formation starts and develops. Since the time resolution of the pulse generator is in the ps, the time resolution of the whole setup is determined only by the total duration of the fluorescent pulse and is equal to ~20 ns.

3. Results and discussion

3.1. Spatial beam properties of pure Rhodamine 6 G dye illumination source

The spatial, spectral and temporal properties of the illumination beam are significantly changed during the propagation through the setup. The first significant transformation takes place in the Second Harmonic Generator (SHG) unit, that converts the light from IR (λ= 1064 nm) into the green wavelength (λ= 532 nm) using nonlinear crystals. After this transformation, the beam profile and temporal characteristics remain quite unchanged. The second significant transformation occurs in the fluorescent converter, where the coherent green light is transformed into the incoherent fluorescent light. An image of the converter is shown in Figure 4(a). The fluorescent dye solution is contained in a rectangular glass cuvette of outer dimensions 10 × 10 × 5 mm^3, half-filled with fluorescent dye solution. The green SH laser beam is focused on to the surface of fluorescent dye solution (green cylinder shown in Figure 4(b)). Because the green laser beam is strongly absorbed by the fluorescent dye, the beam propagates only to a ~30 μm depth into the solution, where it is completely absorbed by the dye. Therefore, we have a disc-like volume of the fluorescent dye of thickness of several tens of micrometres, which is emitting incoherent fluorescent light within a broad wavelength spectrum in all possible directions.

Some of the fluorescent light, which is emitted from a disc-like illuminated volume at the interface between the air and Rh6 G dye solution, is captured by the lens L3 in Figure 1. The diameter of this disc-like volume is equal to the 1 mm diameter of the illuminating green light beam and the height of the disc is equal to the penetration length of the green beam, which is around 30 μm. The image of the fluorescent light-emitting disc-like volume is then projected using the lens L4 in Figure 1 onto the entrance aperture of the fibre coupler.

The lens L3 is a small half-ball lens, which is attached to a thin glass substrate with a thickness of 0.5 mm (serving as a holder) and placed just behind the dye-cuvette wall at a distance of about 3 mm from the interface of the glass-dye solution. This is shown in more detail in the simulation snapshot in Figure 4(b). The separation of 3 mm is the closest distance we could obtain in our setup due to hardware-mounting limitations. This half-ball lens collects the emitted light at an acceptance angle of ~90^o with respect to the beam propagation direction.

The fluorescent light is actually emitted from a disc-like volume of the Rhodamine 6 G solution with ~ 1 mm diameter and 30μm height. The emission is not uniform, because the light is continuously absorbed when propagating from the top air-Rhodamine solution interface in the interior of the solution. For these reasons, the intensity beam profile of the emitted fluorescent light is distorted into a thin line.

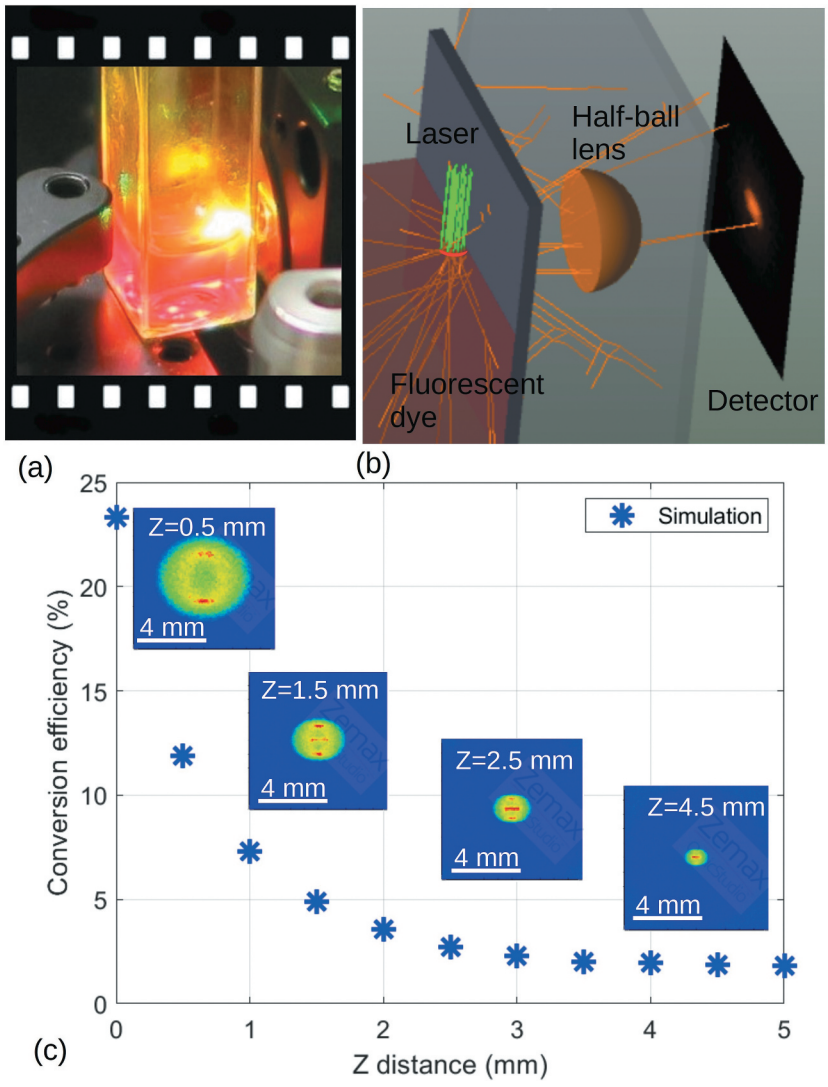

Figure 4. (Colour online) (a) Photo of a Rh6 G fluorescent dye emission in the cuvette. (b) 3D simulation scheme of 532 nm pulsed laser light illumination of the fluorescent dye and collecting the emitted fluorescent light by the half-ball lens. The excitation laser light is shown with the green lines and fluorescent emission with the dark yellow lines. The red line under the green lines represents the edge of the illuminated dye that emits fluorescent light. c) The dependence of the calculated light-to-light conversion efficiency on the position of the half-ball lens with respect to the emission point in the fluorescent dye solution. The inserted panels show the calculated profiles of the emitted fluorescent light at the focal point of the half-ball lens as a function of the lens position with respect to the illumination source.

We use Zemax modelling software (Zemax, OpticStudio Demo) to simulate the efficiency of the illuminating system starting from the dye converter. The geometry of the simulation model is presented in Figure 4(b). The excitation beam is a top-hat beam of 1 mm in diameter and is propagating vertically downwards. The beam hits the horizontal air-Rh6 G interface at a point, situated at 0.5 mm from the cuvette's wall. This position is selected for maximum collection of the emitted fluorescent light by the half-ball lens. We consider a one-to-one Rh6 G conversion for the green light (λ= 532 nm), meaning that each green photon of the excitation beam is absorbed and re-emitted as a single, red-shifted photon from a broader band spectrum. In the simulation, we mimic a cuvette's wall between the florescent media and the half-ball lens and glass substrate where the half-ball lens is considered as an element with transmission of T= 0.95. We consider the collected light intensity at the focal plane of the half-ball lens presented as an orange spot on black screen. The simulations are performed by varying the position of the half-ball lens attached to the glass between 0 mm (the glass wall of the cuvette touches the glass attached to the half-ball lens) and 5 mm with a step of 0.5 mm. One million rays are used for each simulation.

The ratio between the total intensity of the captured fluorescent light in the focal plane and total intensity of incident beam is calculated and is called "a conversion efficiency". Figure 4(c) shows the calculated conversion efficiency as a function of separation of the half-ball lens from the cuvette's wall. The conversion efficiency decreases nonlinearly from about 23% at 0 mm separation to about 1% at 5 mm separation.

The beam profile at the photo-detector also depends on the position of the half-ball lens and changes from a circular-like at 0 mm separation, to the elongated elliptical-one at 5 mm separation, as shown in Figure 4 (c). This is indeed what we observed also in the experiments. To improve the wave-front properties and to convert the elliptical beam into Gaussian-like beam, the multimode fibre is used. The focal plane of the half-ball lens (L3 in Figure 1.) is imaged using a lens (L4) with 10 mm focal distance into a multimode coupler, connected to the multimode fibre with visible range transmission band. The other end of the fibre has a collimator attached. During the beam propagation through the fibre, it becomes homogenised and obtains the super-Gaussian shape, shown in Figure 5(a). This profile is measured with a CCD camera (Pixelink camera, pixel size 6.7 μm, located just behind the multimode fibre collimator. One can see that the intensity is indeed redistributed homogeneously over all beam profile and the original ellipticity is eliminated. The beam has a nice super-Gaussian shape.

The suitable fitting function for the normalised beam intensity profile along the x-axis in **Figure 5(a)** is a super-Gaussian of the 5^{th} order, described with the following formula:

$$I(x) = a_1 exp(-((x-b_1)/c_1)^2) + a_2 exp(-((x-b_2)/c_2)^2) + a_3 exp(-((x-b_3)/c_3)^2) + a_4 exp(-((x-b_4)/c_4)^2) + a_5 exp(-((x-b_5)/c_5)^2) \quad (1)$$

Here $I(x)$ is the normalised intensity, normalised to the maximum intensity at $x = 0$. The unit-less coefficients $a(i)$ for the best fit are $a_1 = 0.3069$, $b_1 = -2.44$, $c_1 = 0.7863$, $a_2 = 0.8068$, $b_2 = 1.45$, $c_2 = 1.644$, $a_3 = 0.8224$, $b_3 = -1.039$, $c_3 = 1.703$, $a_4 = 0.2412$, $b_4 = 2.874$, $c_4 = 0.7262$, $a_5 = 0.1531$, $b_5 = -2.983$, $c_5 = 0.3383$. One of the explanations why the beam profile is converted into super-Gaussian shape instead of low-order super-Gaussian is that the beam is sent into the fibre at a small angle. In this case, the number of skew-rays is increased until the output beam transformed into a high-order super-Gaussian profile.

After exiting the collimator, the beam propagates through the notch filter and a lens L5, as shown in Figure 1. The lens L5 is adjusted along beam propagation

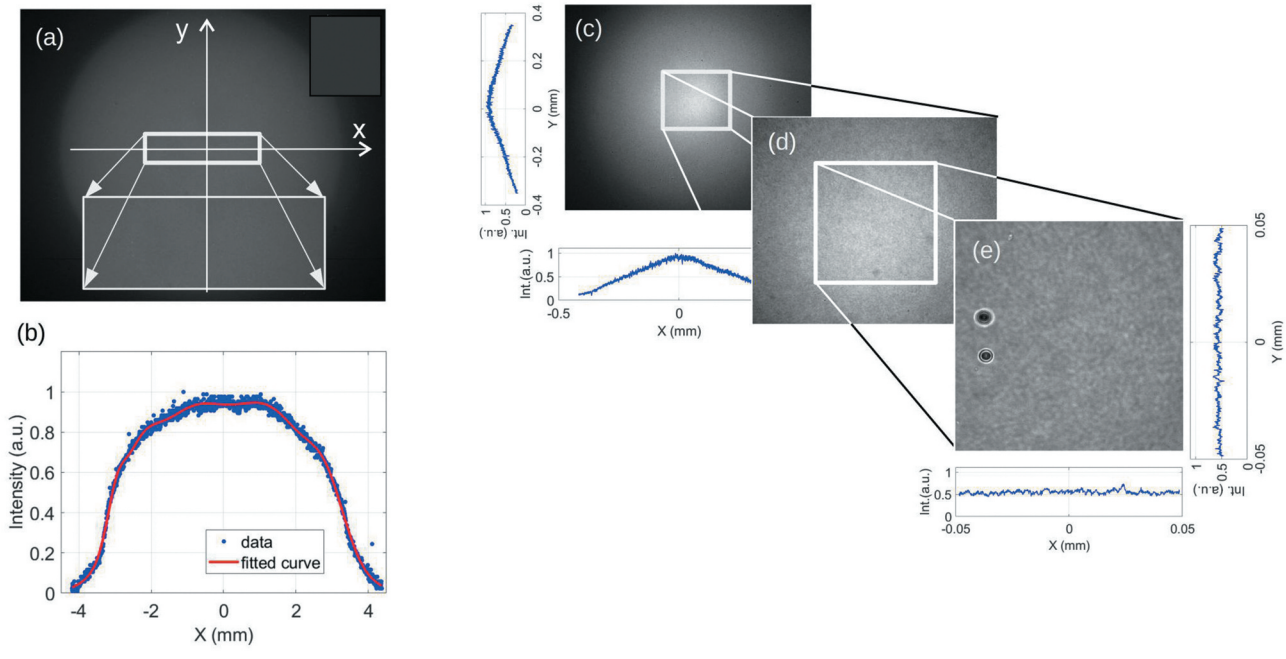

Figure 5. (Colour online) (a) A photograph of the beam profile at the fibre output (at the collimator exit). The image size is 8.6 mm $\times$ 6.8 mm. (b) The cross-section of the intensity beam profile $I(x)$. The best-fitting function is super-Gaussian beam of the 5^{th} order. (c) A photograph of the beam profile at the focal plane. The image obtained with 20 $\times$ objective. The image size equals to 0.8 mm $\times$ 0.7 mm. (d) The same beam profile as in case (c) but obtained with 60 $\times$ objective. The image size equals to 0.28 mm $\times$ 0.23 mm. (e) A sub-image of the image in (d) with the image size of $\approx$ 100 μm $\times$ 100 μm.

axis such that the sample is illuminated with the maximum irradiance. The beam profile of the focused super-Gaussian beam is shown in Figure 5(b). The image is taken using the 20 × magnification air Nikon objective. The obtained beam diameter at the focal plane is about 0.8 mm. One can see that the super-Gaussian beam profile is substantially changed after passing through the lens L5 and the light intensity is concentrated around the axis of the beam, as can be seen from the cross-sections in Figure 5(c). The super-Gaussian beams are acting differently from the Gaussian ones when passing through the lens. This change of the intensity distribution can be explained if we consider the Fourier-transformed profile of the Gaussian beam. This profile contains a centre-part and rings with alternating phase in the Fourier space. In the beginning, the amplitudes contributed by the rings have the opposite signs. After propagating some distance, the central part gets approximately in phase with the first ring in the Fourier space. As a result, a peak intensity is accumulated at the centre, because the total power is conserved the beam area has to become smaller [30].

Moreover, for imaging application, the super-Gaussian beam shape is preferable over the Gaussian or other beam shapes for a homogeneous sample illumination. The better quality of the illumination, the more trustworthy results are obtained from the image analysis. The proposed illumination optics will still work for a microscope application, when the study area is small, i.e. of a fraction of a millimetre. In Figure 5(d,e) one can see the illumination of the field of view, of typical dimensions for our studies. In the image in Figure 5(d), the field of view equals to 0.28 mm × 0.23 mm and for (c) ≈ 100 μm × 100 μm. One can see that the cross-sections (x and y) of Figure 5(e) have rather flat intensity lines. The observed intensity variations are within 10%, observed as a "grainy" structure in the zoomed image in Figure 5 (e). These variations of illumination intensity are due to the partial coherence of the illumination beam. We found in our experiments that even in the cuvette filled only with the fluorescent dye solution, one could obtain lasing at sufficiently strong excitation pulses. Moreover, we found that lasing from Rh6 G solution depended strongly on the position of the illuminating beam, discussed in the next section.

3.2. Lasing from cuvette containing pure Rhodamine 6 G dye

We observed that temporal properties and coherence of the fluorescent light generated from cuvette containing pure Rh6 G solution in ethanol depended critically on the position of the excitation beam in the cuvette. Figure 6(a,d) present the photographs of two different positions of the excitation beam (coming from above). In (a) the beam is positioned very close to the exciting wall of the cuvette, whereas in (d) it is positioned further away from the wall. The fluorescent light shows quite different spectral and temporal properties, compared in the panels (b), (c), (e) and (f) for the same excitation pulse energy. When the excitation beam is focused close to the exiting wall, the emitted spectrum shows typical broadband fluorescent radiation, as measured using the imaging spectrograph (Andor Shamrock SR500i – D1). One can see that fluorescent emission spectrum lays in the range from 570 nm to 690 nm with the peak at 584 nm. The spectrum is slightly shifted towards the IR region in comparison to the Rh6 G-water mixture, due to the very high concentration of the dye. We have checked that the fluorescent spectrum of very diluted dye shows the same spectra as published in the literature. There are several small peaks superposed to this broadband fluorescent spectrum, evidence of the onset of lasing, as explained in the continuation.

When the excitation beam with the same pulse energy is illuminating Rh6 G solution away from the exiting wall, the detected spectrum of the emitted light changes significantly, as shown in Figure 6(e). The broadband fluorescent spectrum gets narrower, and distinct emission lines appear on top of the maximum emission. This is a clear evidence of the onset of lasing, where the glass cuvette serves as an optical resonator, thereby providing an optical feedback and stimulated amplification of light. When the excitation energy is increased, the intensity of the lasing lines increases as well. A possible mechanism that would trigger lasing of the dye in a cuvette is Amplified Spontaneous Emission (ASE), also called mirror-less lasing [31]. In ASE, the optical gain of a system is so large that it results in coherent amplification of light in dense dispersion of optical emitters, which have overlapping optical fields. When the Rh6 G solution is illuminated very close to the exiting wall, the lasing was not observed. We conjecture the lasing is suppressed, because the path of light from the point of excitation to the exit wall is much shorter and optical amplification is too weak to trigger the lasing.

The conversion of the narrow excitation laser line into broadband fluorescence emission is also accompanied with a significant change in emitted pulse duration. The picosecond green excitation pulse of the excitation light is transformed into nanosecond-long fluorescent pulse, shown in Figure 6(c). This is because of the light conversion dynamic properties of the fluorescent dye and their electronic transitions. The duration of the converted pulse is measured with ultra-fast broadband

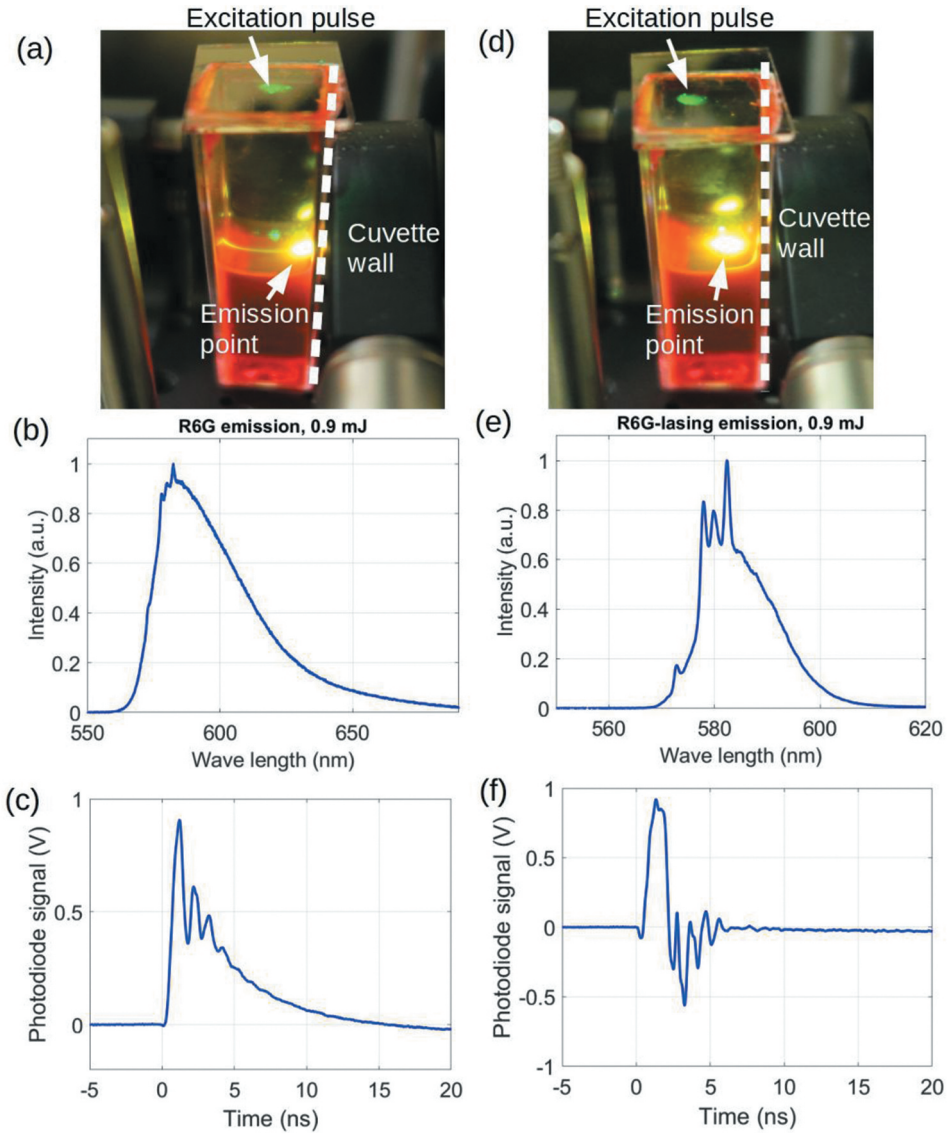

Figure 6. (Colour online) (a–c) Properties of the Rh6 G solution below the lasing threshold. (a) Photo of a cuvette with Rh6 G solution, where the green excitation beam (bright yellow spot) is positioned close to the wall of the cuvette, decreasing the probability for lasing. (b) The measured emission spectrum of the cuvette with Rh6 G dye dissolved in ethanol, below the lasing threshold. The spectral bandwidth is between 570–650 nm, with the peak at λ= 584 nm. Small additional peaks at the maximum of emission indicate the onset of lasing. (c) Time dependence of the intensity of light emitted from cuvette with Rh6 G in ethanol solution. The oscillations are due to "ringing" of the photo amplifier. (d-f) Properties of the Rh6 G solution above the lasing threshold. (d) Photo of a cuvette with Rh6 G solution, where the green excitation beam is positioned away from the wall of the cuvette. At this position of the beam the probability for lasing is enhanced. In this case the cuvette starts lasing, evident from the spectrum shown in (e). (e) The measured emission spectrum of Rh6 G above the lasing threshold, when the excitation spot is moved away from the wall of the cuvette. The spectral bandwidth is 570–600 nm. (f) Time dependence of the intensity of light emitted from the cuvette with Rh6 G in ethanol solution above the lasing threshold. For all presented cases the energy of the green excitation pulse is 0.9 mJ.

photo-detector (Menlosystems gmbh APD210, wavelengths 400–1000 nm, frequency 1–1000 MHz) connected to the 4 GHz oscilloscope (MS09404A, Agilent Technologies).

Below the lasing threshold of the cuvette with Rh6 G solution the full emission duration of the light pulse is about 20 ns and the half-width of the signal corresponds to about 5 ns. For the dyes emitting in the visible range, the duration of 20 ns is a typical value of the fluorescent intensity decay. However, when the cuvette starts lasing after the excitation spot is moved away from the wall, pulse duration narrowing, characteristic of lasing regime, is clearly observed, as shown in Figure 6(f). Unfortunately, the measurement of pulse duration is not reliable in the range of 1 ns due to the ringing of the photo amplifier used to measure the pulse duration.

3.3. Spectral and temporal beam properties of random laser illumination source

The spectrum of light emitted from the random laser converter is quite different, compared to the light emitted from the cuvette with pure Rh6 G solution in ethanol, and is presented in Figure 7(a). Several lasing lines are observable, clear indication of random lasing. This change in spectrum is also reflected in the duration of the random lasing light emission, presented in Figure 7(b). The emitted pulse duration is below 1 ns and is difficult to determine accurately due to bandwidth limitations of the photo amplifier.

3.4. Comparison of illumination stability and brightness

One of the important aspects of the constructed illumination source is its stability over a long period of time. The long-term stability is important because a large amount of data is acquired in the experiments to improve the statistics. In a typical experiment, we take an image every 2 s and we collect several thousand images, adding up to multiple hours of the acquisition time.

There are two main contributors to the system stability: the photobleaching of the fluorescent dye and the

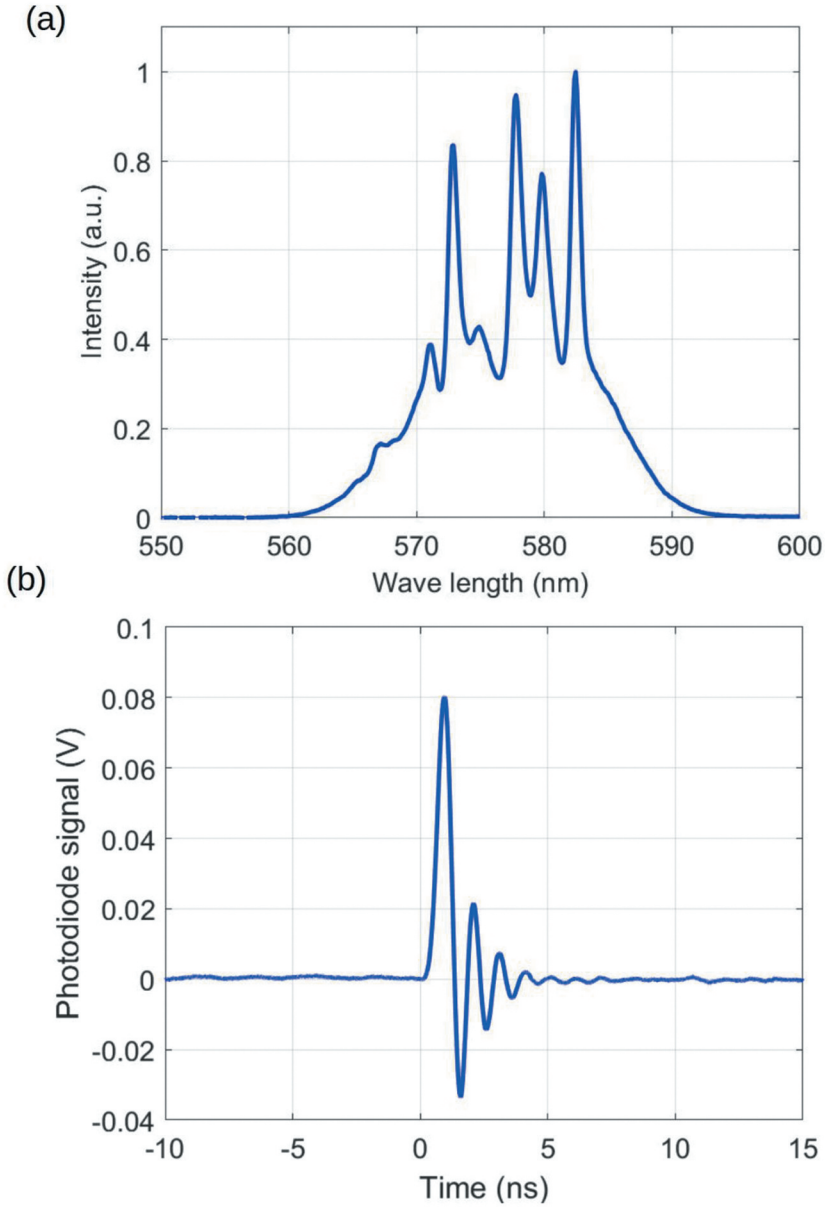

Figure 7. (Colour online) (a) The spectrum of the emitted light from the random laser illumination source. The energy of the 532 nm excitation pulse is 0.7 mJ. (b) Time dependence of the light pulse, emitted from the random laser illumination source. The energy of the 532 nm excitation pulse is 0.7 mJ.

time-stability of the Ekspla SH laser unit. These two contributions are measured simultaneously. A part of the SH light is reflected by a glass substrate into the energy metre (EM-USB J-10MB-HE, Coherent). The rest of the light is forwarded into the dye cuvette or random laser cell. The laser is operated at 10 Hz frequency. The energy of the laser is equal to 0.1 mJ. The Andor camera is acquiring images at the same time as the energy metre is taking the measurements. A set of 150 images are collected with 20 s delay and analysed, roughly equalling to 50 min of the acquisition time. The first measurement is considered as a reference. It is subtracted from all subsequent measurements for both energy-metre and Andor camera. The measurements are grouped in buckets, covering the time duration of 3 min of the experiment.

In Figure 8 one can see the time dependence of the converted light for three different regimes: (i) fluorescent emission from Rh6 G solution in ethanol below the lasing threshold, (ii) the same as (i) but now in the lasing regime, and (iii) random laser emission. The measurements have shown that SH is very stable in the measured period of time. During the measurement, the energy fluctuations did not exceed 1%, as presented in the inset to Figure 8.

One can see from Figure 8 that below the lasing regime, the intensity of light generated from the Rh6 G cuvette follows the excitation laser trend and is quite stable. It does not show any visible light intensity decrease during the measurement, which is an excellent characteristic. The standard deviation of the measurement is below 1%. The prepared Rh6 G samples are very stable and can sustain the long hours and weeks of the measurements.

The stability of light emission from the Rh6 G cuvette in the lasing regime is significantly worse, as one can see from the green symbols in Figure 8. During 1 h of operation, the drop in the emitted intensity is nearly ~6%, due to photo-bleaching of Rh6 G under an intense light. The stability of the lasing intensity of Rh6 G is about 2%. In principle, the intensity drop over period of time can be always compensated by the energy increase of the SH Ekspla unit or by the volume increase of the fluorescent dye solvent. The output stability of random laser is in between the non-lasing and lasing regimes of Rh6 G in ethanol, and the decrease of the output light is around ~4% during 1 h of continuous operation. The stability of this source is around ~2%. The further photo-bleaching can be compensated by the increase of the pumping energy. However, at the pulse excitation energies of 0.7–1 mJ the further increase of the pumping energy leads to the breakdown of the random laser cell material.

Figure 9 shows the brightness of different illumination sources, measured in number of detected photons per pixel area, depending on the energy of the excitation pulse. The measurement is done using the Andor camera. The microscope is focused on a glass cell with 10 μm thick spacing, made of two bare glass substrates and filled with isotropic liquid, in this case, immersion oil.

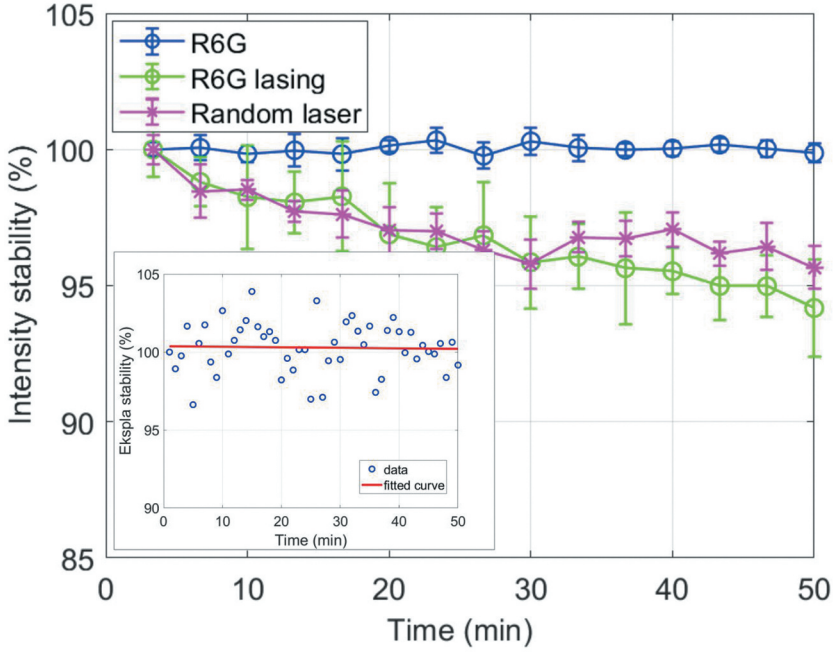

Figure 8. (Colour online) Stability of the illumination converters. The measurements are done at 10 Hz laser repetition frequency. The inset shows the time dependence of the pulse energy from the Second Harmonic Unit measured over about 50 min.

The lowest brightness is measured for pure Rh6 G solution in ethanol in excitation conditions below the lasing threshold. When the excitation beam is moved away from the wall to induce lasing, the brightness is increased nearly ten fold. This is understandable, as the stimulated emission of light bouncing between the walls of the cuvette directs the energy into the lasing direction, thereby increasing the brightness of the converter. The brightness of the random laser converter is in between the non-lasing and lasing regimes of Rh6 G solution in ethanol. A similar trend is observed for the ageing of the output intensity with time, presented in Figure 8.

3.5. Comparison of image quality in terms of speckles

The graininess of the acquired images is the most important parameter determining the image quality in our fast imaging applications. The reason is in our study of the formation of topological defects during the fast passage through the phase transition. Defects are expected to appear as tiny, diffraction limited "grains" or irregularities in acquired images, similar to speckles that appear when the illumination source is partially coherent. This means that any additional image graininess due to the speckle structure of the illumination light is of utmost importance and should be minimised as much as possible. We expect that the coherence of the light source shall play the most important role; the fluorescence source in the non-lasing regime should give the best, speckle-free image, while the increasing coherence of the illumination source should deteriorate the image quality due to the appearance of speckles.

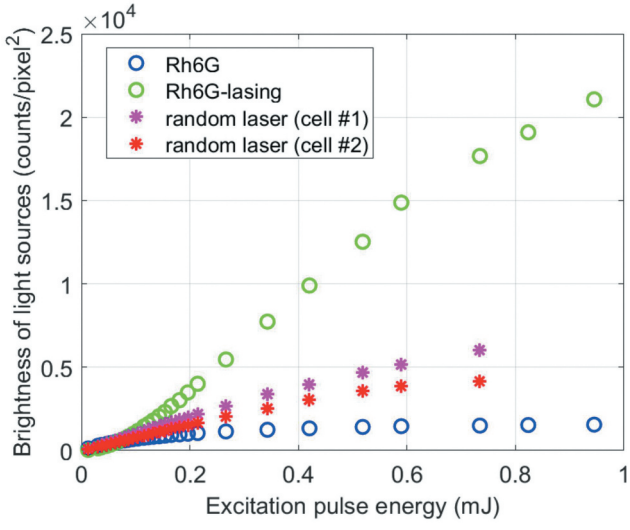

Figure 9. (Colour online) Brightness of different illumination converters captured by the camera and measured in acquired photon counts per pixel, as a function of the energy of excitation pulses. The error bars for random laser and Rh6 G emission correspond to the data point on the graph.

We, therefore, compare the quality of images, taken with three different types of illumination sources: (i) Rh6 G solution in the non-lasing regime, (ii) Rh6 G solution in lasing regime, and (iii) random lasing regime from Rh6 G/TiO2 dispersion. We are using a standard measure for the graininess of the acquired image by calculating the speckle contrast of the image, $C = \sigma/\langle I \rangle$, where $\langle I \rangle$ is the average value of the light intensity detected across the pixel array and σ is the standard deviation for the array (i.e. RMS roughness of the intensity across the pixel array). Note that, for our imaging application the lowest possible value of C at a reasonably high brightness is preferable.

Figure 10 shows images taken under the microscope focused onto a glass cell filled with isotropic and transparent oil, thereby showing the uniformity of the illumination source. The average intensity in all panels has been normalised to 1, to be able to compare the RMS "roughness" of the light intensity profile for each type of illumination. Figure 10(a) shows the normalised intensity profile for Rh6 G illumination source taken under the non-lasing conditions in the cuvette. The average intensity of the image is 1526 counts, whereas the RMS roughness corresponds to 61.3 counts. This corresponds to the speckle contrast of $C = 0.04$.

Figure 10(b) shows the normalised intensity image for the Rh6 G illumination source, now in the lasing regime. Note that in the lasing regime several lasing modes are evident from the spectral analysis shown in the inset to Figure 10(d). As a result of the crossover to the lasing regime, the speckles are clearly observable from the normalised image in Figure 10(b). Although the brightness of the illumination increases to the average of 2553 counts, the average roughness and the speckle contrast increases to $C = 0.05$ as well. Here the ND filter with OD = 1 is applied; hence, the actual light intensity is higher than measured by the camera.

Figure 10(c,d) shows the normalised intensity images of two different random laser cells. The difference between these two cells is the time when the measurement is carried out. The cell 1 is measured right after filling it. The cell 2 is measured after all day of the measurements, when ethanol starts evaporating. The average intensities of the two images are 6030 counts for panel (c) and 4170 counts for panel (d). The corresponding RMS roughnesses are clearly larger compared to pure Rh6 G below and beyond the lasing regime. For the random lasing cell 1 we calculate the speckle contrast of C= 0.037, whereas for the random lasing cell 2 we calculate the speckle contrast of C= 0.16.

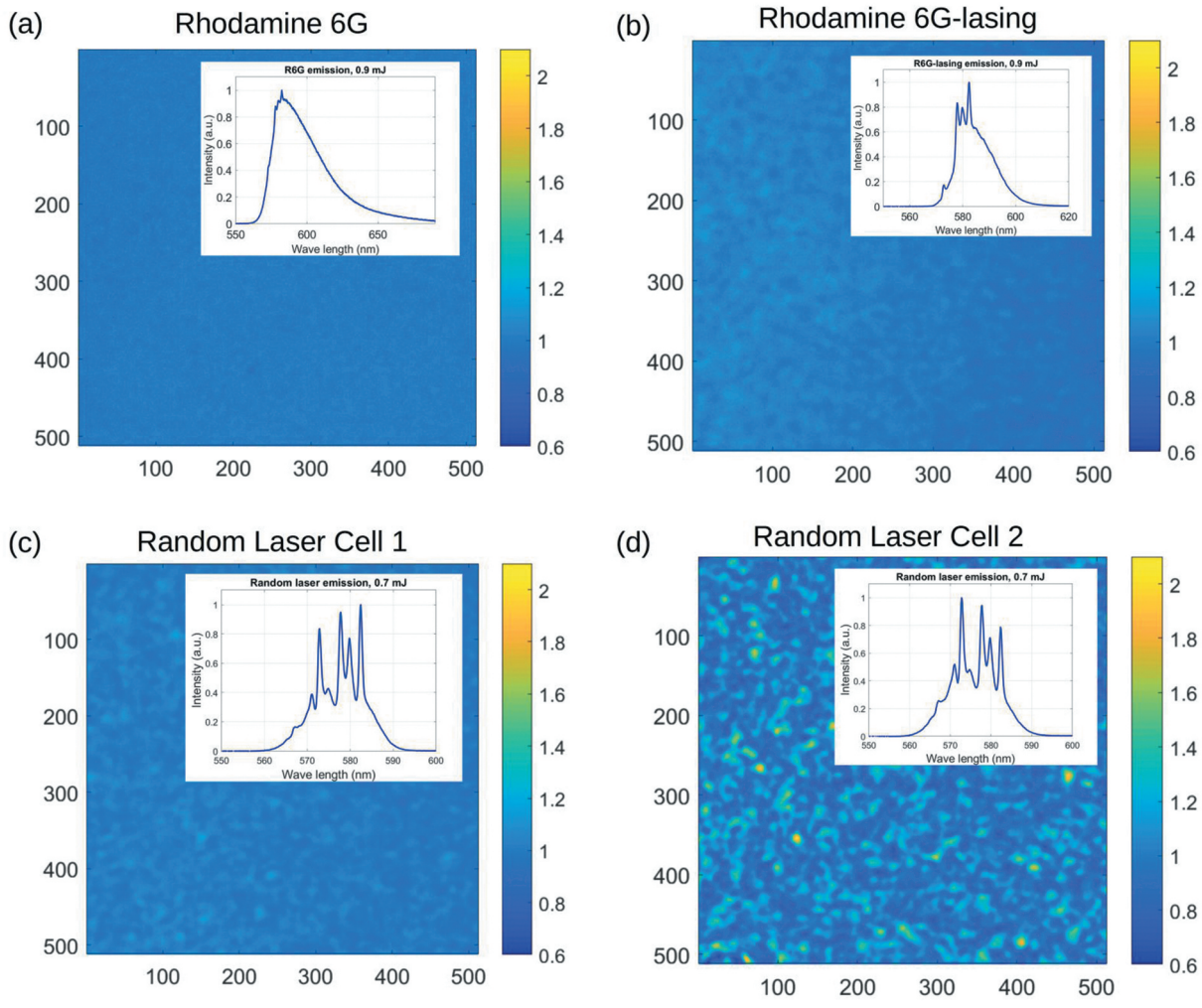

Figure 10. (Colour online) The images are showing the uniformity of the illumination of the camera sensor for different illumination converters. (a) Pure solution of Rh6 G in ethanol, placed in a cuvette. The excitation pulse energy is 0.9 mJ, the cuvette is in the non-lasing regime. The average intensity of pixels is 1526 counts. The image is normalised to this average intensity. The inset shows the corresponding spectrum of the illumination light. (b) Pure solution of Rh6 G in ethanol, placed in a cuvette. The excitation pulse energy is 0.9 mJ, the cuvette is now in the lasing regime. The average intensity of pixels with ND (OD = 1) is 2553 counts. The image is normalised to this average intensity. The inset shows the corresponding spectrum of the illumination light. (c) The image is taken by the random laser illumination converter, cell 1. The average intensity of pixels is 6030 counts. The image is normalised to this average intensity. The inset shows the corresponding spectrum of the illumination light. The excitation pulse energy is 0.7 mJ. The measurement is done on a 'fresh' random laser sample. (d) The image is taken by the random laser illumination converter, cell 2. The average intensity of pixels is 4170 counts. The image is normalised to this average intensity. The inset shows the corresponding spectrum of the illumination light. The measurement on the cell is done after all-day operation. Its properties seem to change due to the evaporation of ethanol. The excitation pulse energy is 0.7 mJ. The size of all images is $\approx 55\ \mu\text{m} \times 55\ \mu\text{m}$.

These results clearly show the overall tendency for different illumination setups. This is presented in Figure 11, where the speckle contrast is shown as a function of the excitation pulse energy and corresponding brightness of our various light converters. We obtain the best, stable and speckle-free image using pure Rh6 G cuvette, operating below the lasing threshold. The speckle contrast of this source is independent of the excitation energy above ~0.2 mJ. The operation of this source relies on careful adjustment of the position of the green excitation beam and the energy level of the excitation pulses and should not exceed the lasing threshold of the cuvette. Once finely adjusted, such an illumination converter provides high optical quality (speckle free) and very stable operation.

By transiting into the lasing regime of the Rh6 G cuvette, the brightness of the illumination source increases, but at the expense of image quality and the appearance of speckles. The speckles are clearly observable above the lasing threshold and the quality of the image becomes slightly "grainy", as evidenced by higher value of the speckle contrast C shown in Figure 11.

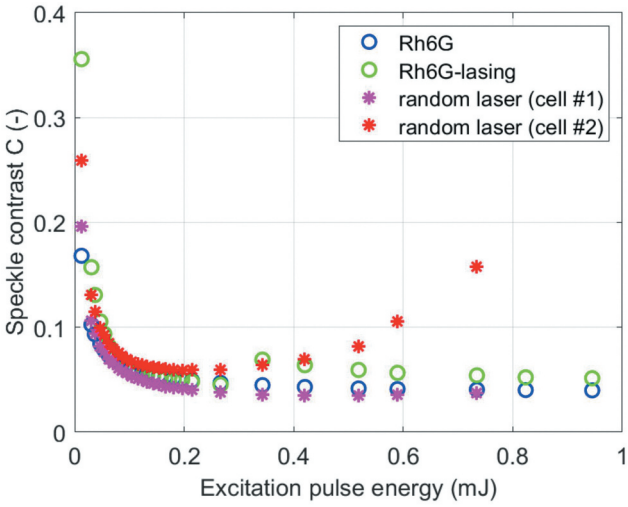

Figure 11. (Colour online) Speckle contrast $C = \sigma/\langle I \rangle$ for different illumination converters, calculated from the acquired images at different excitation pulse energies.

The graininess of the image obtained with Rh6 G above lasing threshold is comparable to the graininess of a fresh random laser cell (C= 0.04 and C= 0.037, respectively). The deterioration of the image quality is even more pronounced, when we use the random lasing source after a day of operation when ethanol starts evaporating. The ethanol evaporation does not affect the light brightness that much in comparison to the graininess appearance and enhancement of their contrast. As an example, one can see the fresh random laser cell in Figure 10(c) and enchantment of the "grains" after a day of operation in Figure 10(d) with contrast of 0.16. The deterioration of the speckle contrast and the enchantment of speckles over a period of time make the random laser light source less attractive for long-term measurements.

Therefore, Rh6 G cuvette presents the most powerful, stable and homogeneous-light source for imagining applications with very low level of coherence and speckles. The illumination light coherency ("grains") can actually be tuned from the fully incoherent to slightly coherent light by placing a pumping laser beam at a given distance with respect to the cuvette's wall. In the most "coherent"-case the grain structure is comparable with a fresh random laser cell, when the solution is present in the random laser cell. Then, the light intensity of Rh6 G is about five times higher rather than random laser illumination. The stability of Rh6 G enables long-term experiments running over the 3–4 weeks time.

3.6. Crossed-polarisers light microscopy

The designed setup is constructed and used to study the temporal dynamics of the orientational disorder in the nematic liquid crystal during rapid temperature quench. The liquid crystal is locally heated by laser light and melted into an isotropic island, as shown in Figure 12 (a). After switching-off the heating laser light, the isotropic island starts cooling down and eventually reaches the temperature of the phase transition to the nematic phase. At that moment, the nematic phase nucleates in a form of "frozen" domains well separated from each other, as shown in Figure 12(b). This is because of the first-order nature of the isotropic-nematic phase transition, where both phases coexist in a narrow temperature region. While the LC is cooled through this coexistence region, islands of nematic phase are spontaneously formed in the isotropic surroundings, because of the specific free-energy energy landscape near the isotropic-nematic transition temperature.

After further cooling down, the number of nucleated domains remains unchanged, but they are now growing in size, until they meet and start colliding. Because the local alignment of the nematic liquid crystal is different in neighbouring domains, a defect line or wall is formed at the interface of two touching domains. At this moment, a dense network of defect lines is formed in the sample, as shown in Figure 12(c,d). In the course of time, this network of defect lines annihilates and the domains grow at the expense of neighbours, which is called the coarsening dynamics (Figure 12(d-f)).

We are interested in a related mechanism of defect production, while crossing the isotropic-nematic phase transition, which is called Kibble-Zurek mechanism of defect production. This mechanism was originally proposed by Kibble [32] to describe the production of monopoles, cosmic strings and textures in early Universe and was subsequently reformulated by Zurek [33,34] for defect production in condensed matter. Kibble-Zurek mechanism has been extensively studied in liquid crystals both in experiments [35–38] and using numerical approach [39,40]. Most of the experiments were focused on the isotropic-nematic phase transition and **analysed** the domain size distribution, the effect of cooling rates on defect nucleation and later stages of coarsening and annihilation. Typical cooling rates were of the order of $1\text{K} - 10\text{K/s}$, which is in our opinion too slow to separate the nucleation mechanism due to the first-order phase transition from true Kibble-Zurek mechanism. We estimate that cooling rates of at least 100.000K/sare required to suppress defect production due to first-order nature of the isotropic-nematic phase transition.

In our quenching experiments, we easily achieve cooling rates of 40000K/s. During such fast cooling, Kibble-Zurek mechanism is expected to bee seen in a very short time, typically in 1 ms after the heating laser light is switched off. To take images of these rapidly

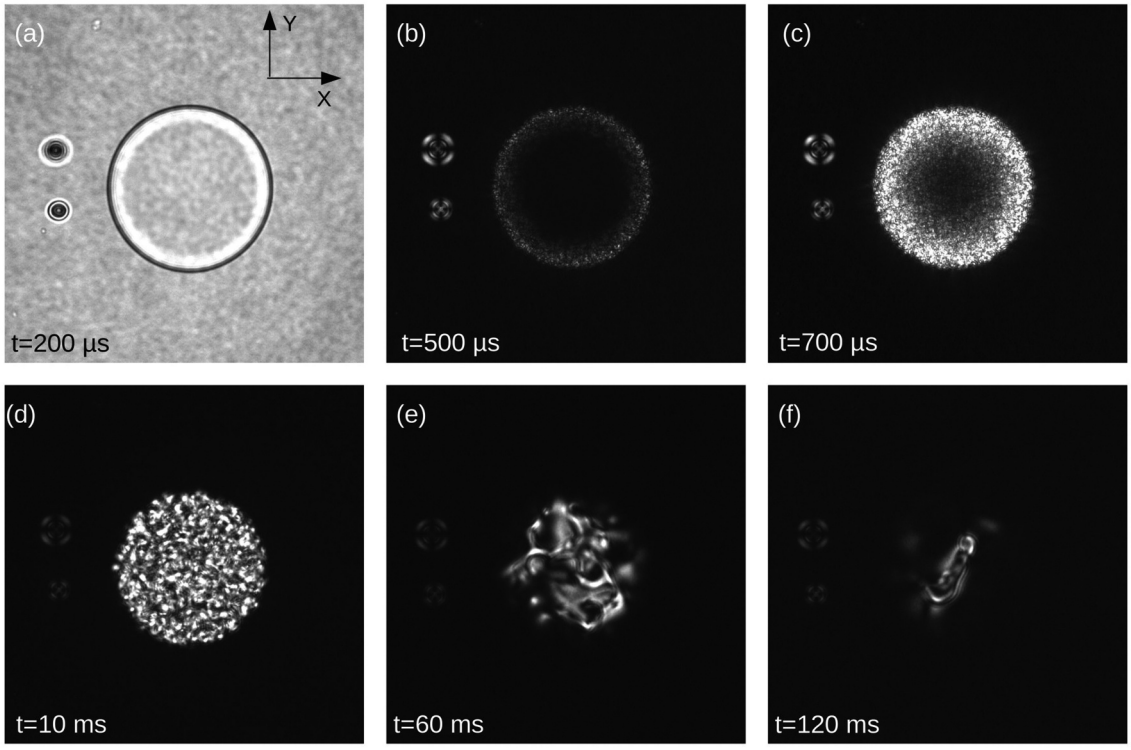

Figure 12. (Colour online) a) A photograph of an isotropic island formed by λ= 532 nm laser heating of the nematic liquid crystal due to opto-thermal effect. The image is taken 200 μs after the heating laser is switched off. b), c), d), e), f) The photographs of the nematic liquid crystal texture at some selected times after switching off the heating laser. The images are taken for the following times: 0.5, 0.7, 10, 60 and 120 ms, respectively. The image sizes are $\approx$ 100μm $\times$ 100μm.

appearing domains, we need a fast imaging system. Fast imaging is indeed provided by our 20 ns pulsed illumination source, acting as a nanosecond flashlight, illuminating the defect texture instantly. The image is taken by a sensitive camera, acquiring the image in a much longer time interval. However, most of the acquisition time there is no light that can expose the imaging sensor. Therefore, it is clear that our 20 ns illumination source will provide unprecedented time resolution for acquiring the image, giving excellent sharpness of the acquired image and absolutely controlled time delay between the start of the cooling-down of the sample and the moment the image is taken.

The formation of nematic domains is best observed between two crossed polarisers, because the nematic domains are birefringent, whereas the isotropic surrounding is not. Crossed-polarised light is, therefore, a contrast-enhancing technique that greatly improves the quality of the image of birefringent materials.

Figure 12 shows a series of snap-shots of the liquid crystal textures, taken at precisely delayed moments after the quench started. Each panel is taken in a separate experiment and we can control the time delay of that particular snapshot below 1 μs. The time counting starts from the moment the heating laser is switched off. Over the first 500 μs (Figure 12 (a)) the isotropic island is cooling down with no apparent optical change, because the temperature of the material within this island is above the isotropic phase transition temperature [29]. The island, therefore, remains unchanged until the coolest part reaches the melting point, for the liquid crystal 5CB used 35°C. The image in panel in Figure 12(a) is taken with a single polariser, else with the isotropic island, we would see only a dark image between crossed polarisers. All other panels in Figure 12 are taken between crossed polarisers. The first small domains of the nematic liquid crystal start to nucleate at the edge of the island (Figure 12(b)), and then they start spreading towards the island centre (Figure 12(c)). The whole process takes only $\sim$ 200μs. The appearance of the first domains at the edge of the island is understandable in terms of the local temperature of the liquid crystal, highest in the centre of the isotropic island and decreases towards 35°C at the edge of the island, where the isotropic phase meets the nematic phase.

In the panels in Figure 12(d–f) taken during the following milliseconds, the large domains and defect lines are formed and later also annihilated. When the large nematic domains are formed they cause a large

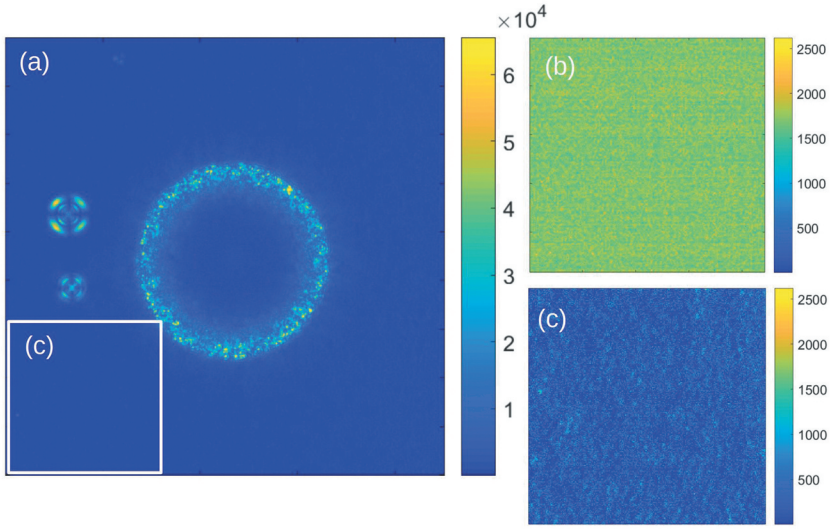

Figure 13. (Colour online) a) An image of liquid crystal quench after t= 500 μs of cooling down. The image sizes is $\approx$ 100μm $\times$ 100μm. b) The enhanced image of the electronic noise of the Andor camera, acquired with no light illumination. The average number of counts, corresponding to electronic noise is 1700. The size of the cropped area is $\approx$ 100μm $\times$ 100μm. c) The enhanced image of the area outside of the liquid crystal quench, indicated by (c) in panel (a). The size of the cropped area is $\approx$ 33μm $\times$ 33μm. The scale in each image is the number of photons detected by the camera at each pixel.

transmission of light through the sample between crossed polarisers, due to the birefringence of the domains. This causes camera over-illumination and the sensitivity of the camera needs to be decreased for the long time delay imaging. This decrease of the camera sensitivity can be seen by the decrease of the light intensity around the spherical micro-particles (for, e.g. Figure 12(c–d)). All liquid crystal defects caused by the fast temperature quench from the isotropic phase annihilate in about 120 ms. In this article, we will not discuss in details the observed creation and subsequent coarsening dynamic followed by the annihilation of defects, as it is the purpose of the upcoming manuscript.

From the images Figure 12(b–f), one can see the excellent image quality and the high contrast obtained. The "graininess" of the image, clearly visible in Figure 13(a) is hardly observable. The crossed polarised image analysis shows that the noise amplitude of the "dark" area of the image is around 3.4%, close to the level of the electronic noise of the camera itself, found to be 2.6%. For this purpose, the image is taken without any illumination as shown in Figure 13(b). The obtained background noise is subtracted from a raw experimental image. The result can be seen in Figure 13(a,c). Figure 13(a) shows the image of the liquid crystal quench after cooling-down period of time t = 500μs. The enhanced image of the background (electrical noise) can be seen in Figure 13(b). The further noise enchantment of the cropped area outside the heated area is shown in Figure 13(c). The noise level (seen as an image graininess) outside the heated area cased by thermal fluctuations of the nematic liquid crystal (Figure 13(c)) is low, i.e. around 200 counts, and 0.5% with respect to the full transmission intensity (~65000 counts).

The most appealing and surprising aspect of our study is that the fluorescent light previously considered to be too weak for illumination systems can be in fact such a powerful light source. It is also interesting to estimate the amount of photons, we are generating from our illumination setup for such low-light phenomena observations. The theoretical estimate tells that the total transmission of our set-up is around ~0.17%. In this estimate we consider the transmission of optical elements: $T_{lens1,2}$= 0.96, T_{fibre}= 0.9, $T_{objective}$= 0.5, $T_{cropped}$= 0.15, T_{image}= 0.03. Here, $T_{cropped}$ stands for the amount of light, cropped from the total beam due to selection of the region of interest in the camera, here it is $\approx$ 100μm $\times$ 100μm. T_{image} stands for the amount of light passing through the crossed-polarisers, seen on the image as a bright area around the defects. In this particular case, the light transmission between crossed-polarisers is equal to 3% (in Figure 7(a)). Considering that the energy of 532 nm pumping SH pulse is $E = 0.7$ mJ, we calculate the number of 532 nm pumping photons by taking $N = E/E_{photon}$, where $E_{photon} = hc/\lambda$, h= $6.626 \cdot 10^{-34}$ m ^{2} kg/s, $c = 3 \cdot 10^8$ m/s, λ= 532 nm, and we have N= 1.9 $\cdot 10^{15}$ green photons hitting the Rh6 G mixture. Taking into account the full setup transmission, the conversion coefficient of the wave-length converter equalled to 0.01 (estimated in the previous section),

and a fluorescent dye conversion coefficient is 0.95 the total amount of photons that reaches the camera is $N_{photon} = 3 \cdot 10^{10}$.

The actual amount of photons in the region of interest detected by the Andor camera (Figure 7(a)) is $N_{measured} = 1.6 \cdot 10^{9}$. The measured amount of photons is calculated as $(signal - background) \times sensitivity/QE$ and integrated over the region of interest, where *signal* is an image acquired by the camera in counts, *background* is an image taken with no light (offset) in counts, $sensitivity = 0.5$ electrons per A/D count and $QE = 0.57$ is a camera quantum efficiency at the wavelength of an interest ($\lambda = 590nm$). The difference between the measured and estimated amount of photons differes by a factor of 20 and can be explained by the fact that for estimation we actually do not know the exact efficiency of the fluorescent light coupling into the fibre.

4. Conclusion

We propose a simple design of the setup for the 20 ns single-shot illumination system for imaging applications. In comparison to the existing designs, this one provides an excellent, speckle-free and high contrast image quality with the exposure duration of 20 ns (5 ns FWHM). The design is based on stroboscopic principle and uses the fluorescent emission from a solution of a fluorescent dye as an illumination source. Surprisingly, the amount of the emitted light is sufficient even for low-light microscopy with sample transmission up to 4%. The setup is remarkably stable over several weeks of continuous experiments and enabled to carry out the full statistical analysis of the observed phenomena by acquiring sequences of tens of thousands of images.

All details of the setup design and its working principles are explained in full detail. The basic spatial, temporal, and spectral properties of the beams are characterised and discussed. The light conversion from green into broad-band fluorescent light in the bulk dye material is modelled and a conversion coefficient is estimated to $\sim$ 1%. The total transmission of all setup components is estimated to $\sim$0.17%. Remarkably, even with such a low system transmission, it is still possible to over-illuminate the Andor camera sensor.

We have compared the properties of Rh6 G built-light source with the random laser illumination source. It is shown that the glass cuvette containing Rh6 G can be tuned from the incoherent to a slightly coherent spectrum of the emitted light by properly positioning the pumping beam with respect to the cuvette's wall. In the most coherent case, the graininess of the light emitted from the cuvette becomes comparable with random laser graininess but the Rh6 G light intensity becomes five times higher than the random laser in this configuration.

Our conclusions are very clear: the use of either fully incoherent light converter based on fluorescent emission from the cuvette filled with Rh6 G or a random laser depends on the demand of the experiment. If the speckles are not so important for the image quality, and the duration of the experiment is short (several hours), then the random laser converter is superior choice due to the very high brightness. However, when the experiment requires the lowest possible level of coherence and image graininess, with several days of stability, then a cuvette filled with Rh6 G solution in the non-lasing regime is a superior choice.

We have demonstrated the working principle of the setup by direct imaging of fast textural transients during the temperature quenching the nematic (5CB) liquid crystal from its isotropic phase. The snapshots of temporal dynamics are displayed in the set of images. The setup allows for capturing a huge number of high-quality images, which are the basis for further graphical analysis to extract the size and number of nematic domains, their growth and statistical analysis. In this kind of experiments, where the illumination should be really smooth across the camera pixels, the incoherent light source based on Rh6 G in the non-lasing regime is the best choice. This will be described in detail in a following-up manuscript.

Acknowledgments

The authors are thankful to Zemax company for providing the Demo version of OpticStudio for the optical simulations. This work of A.R. and I.M. is supported by the Slovenian Research Agency (ARRS) research program P1-0099. The work of U.J. was supported by the Slovenian Research Agency (ARRS) through the contract No. 37473.

Disclosure statement

No potential conflict of interest was reported by the author(s).

Funding

This work is supported by the Slovenian Research Agency (ARRS) research program P1-0099.

References

[1] Mikami H, Gao L, Goda K. Ultrafast optical imaging technology: principles and applications of emerging methods. Nanophotonics. 2016;5(4):497–509.

[2] Scoby CM, Li RK, Threlkeld E, et al. Single-shot 35 fs temporal resolution electron shadowgraphy. Appl Phys Lett. 2013;102:023506.
[3] Goda K, Tsia KK, Jalali B. Serial time-encoded amplified imaging for real-time observation of fast dynamic phenomena. Nature. 2009;458:1145–1149.
[4] Goda K, Tsia KK, Jalali B. Amplified dispersive fourier-transform imaging for ultrafast displacement sensing and barcode reading. Appl Phys Lett. 2008;93 (13):131109.
[5] Matlis NH, Axley A, Leemans WP. Single-shot ultrafast tomographic imaging by spectral multiplexing. Nat Commun. 2012;3(1):1–8.
[6] Diebold ED, Buckley BW, Gossett DR, et al. Digitally synthesized beat frequency multiplexing for sub-millisecond fluorescence microscopy. Nat Photon. 2013;7(10):806–810.
[7] Goda K, Ayazi A, Gossett DR, et al. High-throughput single-microparticle imaging flow analyzer. Proc Natl Acad Sci. 2012;109(29):11630–11635.
[8] Nakagawa K, Iwasaki A, Oishi Y, et al. Sequentially timed all-optical mapping photography (STAMP). Nat Photon. 2014;8(9):695–700.
[9] Tamamitsu M, Nakagawa K, Horisaki R, et al. Design for sequentially timed all-optical mapping photography with optimum temporal performance. Opt Lett. 2015;40(4):633–636.
[10] Wang X, Zgadzaj R, Fazel N, et al. Quasi-monoenergetic laser-plasma acceleration of electrons to 2 GeV. Nat Commun. 2013;4(1):1–9.
[11] Li Z, Zgadzaj R, Wang X, et al. Frequency-domain streak camera for ultrafast imaging of evolving light-velocity objects. Opt Lett. 2010;35(24):4087–4089.
[12] Gao L, Liang J, Li C, et al. Single-shot compressed ultrafast photography at one hundred billion frames per second. Nature. 2014;516(7529):74–77.
[13] Glaeser RM. Stroboscopic imaging of macromolecular complexes. Nat Methods. 2013;10(6):475–476.
[14] Matthews DR, Summers HD, Njoh K, et al. Technique for measurement of fluorescence lifetime by use of stroboscopic excitation and continuous-wave detection. Appl Opt. 2006;45(9):2115–2123.
[15] Yu H, Li B. Wavelength-converted wave-guiding in dye-doped polymer nanofibers. Sci Rep. 2013;3(1):1674.
[16] Horn A. Ultra-fast material metrology. Weinheim: WILEY-VCH Verlag GmbH & Co. KGaA; 2009.
[17] Miyazaki J, Tsurui H, Hayashi-Takagi A, et al. Sub-diffraction resolution pump-probe microscopy with shot-noise limited sensitivity using laser diodes. Opt Express. 2014;22(8):9024–9032.
[18] Raman RN, Negres RA, Demos SG. Time-resolved microscope system to image material response following localized laser energy deposition: exit surface damage in fused silica as a case example. Opt Eng. 2011;50(1):013602.
[19] [cited 2008 Dec 19]; http://news.thomasnet.com/fullstory/led-strobe-light-supports-high-speed-applications-20026321.
[20] Willert C, Stasicki B, Klinner J, et al. Pulsed operation of high-power light emitting diodes for imaging flow velocimetry. Meas Sci Technol. 2010;21 (7):075402.
[21] Elsinga GE, Scarano F, Wieneke B, et al. Tomographic particle image velocimetry. *Exp. Fluids.* 2006;41 (6):933–947.
[22] Pereira F, Gharib M, Dabiri D, et al. Defocusing digital particle image velocimetry: a 3-component 3-dimensional DPIV measurement technique. Application to bubbly flows. *Exp. Fluids.* 2000;29(1):S078–84.
[23] Rose J, Bradbury S, Bond I, et al. Driving LED in a nanosecond regime by a fast operational amplifier. *arXiv preprint arXiv:1011.1954*; 2010.
[24] Mermillod-Blondin A, Mentzel H, Rosenfeld A. Time-resolved microscopy with random lasers. Opt Lett. 2013;38(20):4112–4115.
[25] Hokr BH, Thompson JV, Bixler JN, et al. Enabling time resolved microscopy with random Raman lasing. Sci Rep. 2017;7(1):1–7.
[26] Viehmann W Fluorescent radiation converter. US 4262206 A. 1981.
[27] Butterworth MM, Helbing RP. Fluorescent dye added to epoxy of light emitting diode lens. EP 1021817 A1. 2013.
[28] Harjunmaa H, Ekholm P, Suovaniemi O. Procedure and apparatus for determining the fluorescence of a liquid sample. WO 1992014137 A1. 1992.
[29] Jagodič U, Ryzhkova AV, Muševič I. Localised opto-thermal response of nematic liquid crystal to laser light. Liq Cryst. 2019;46(7):1117–1126.
[30] Paschotta R. Encyclopedia of laser physics and technology. Berlin: Wiley-vch; 2008.
[31] Siegman AE. Lasers. Mill Valley, Calif: University Science Books; 1986.
[32] Kibble TW. Topology of cosmic domains and strings. J Phys. 1976;9(8):1387.
[33] Zurek WH. Cosmological experiments in superfluid helium? Nature. 1985;317(6037):505–508.
[34] Zurek WH. Cosmological experiments in condensed matter systems. Phys Rep. 1996;276:177.
[35] Chuang I, Durrer R, Turok N, et al. Defects dynamics in liquid crystals. Science. 1991;251:1336.
[36] Bowick MJ, Chandar L, Schiff EA, et al. The cosmological Kibble mechanism in the laboratory: string formation in liquid crystals. Science. 1994;263(5149):943–945.
[37] Snyder R, Pargellis AN, Graham PA, et al. Light-transmission study of coarsening in a nematic liquid crystal. Phys Rev A. 1992;45(4):R2169.
[38] Fowler N, Dierking DI. Kibble–Zurek scaling during defect formation in a nematic liquid crystal. Chem Phys Chem. 2017;18(7):812–816.
[39] Bradač Z, Kralj S, Žumer S. Molecular dynamics study of the isotropic-nematic quench. Phys Rev E. 2002;65:021705.
[40] Bradač Z, Kralj S, Žumer S. Early stage domain coarsening of the isotropic-nematic phase transition. J Chem Phys. 2011;135:024506.